crystals

MDPI

Article

Mechanochemical Evolution of $Ni_{50}Ti_{30}Zr_{20}$ Alloy During High-Energy Ball Milling

Thobani Paul Shangase [1], Maria Ntsoaki Mathabathe [2,*] and Charles Witness Siyasiya [1]

[1] Department of Materials Science and Metallurgical Engineering, University of Pretoria, Pretoria 0002, South Africa
[2] School of Chemical and Metallurgical Engineering, University of the Witwatersrand, 1 Jorissen St, Braamfontein, Johannesburg 2050, South Africa
* Correspondence: maria.mathabathe@wits.ac.za

Abstract

The fabrication of NiTiZr alloys by solid-state routes remains challenging due to limited atomic diffusion and the high reactivity of Ti and Zr. Mechanical alloying offers a potential pathway for synthesising such systems; however, complete alloy formation is not always achieved under practical milling conditions. Researchers have infrequently explored the mechanical alloying of NiTiZr, and this study systematically investigates the effect of milling time on microstructural evolution rather than claiming complete alloy synthesis. A high-energy planetary ball mill was used to mechanically process elemental powders of Ni, Ti, and Zr for 5–28 h. The examination revealed that longer milling times resulted in progressive crystallite refinement and increased lattice strain, while particle morphology evolved from irregular to more globular shapes due to repeated fracture and cold welding. After 28 h of milling, limited reacted regions containing Ni, Ti, and Zr were observed (~4.6% area fraction), while most of the powder remained heterogeneous and polyphasic, with no evidence of complete $Ni_{50}Ti_{30}Zr_{20}$ alloy formation. X-ray diffraction showed significant peak broadening without systematic 2θ peak shifts, indicating severe plastic deformation and crystallite refinement rather than definitive solid-solution formation of the allot. Differential scanning calorimetry revealed exothermic thermal events between 300 °C and 470 °C, which are attributed to defect recovery and thermally activated structural rearrangements rather than confirmed martensitic or crystallisation transformations. These results demonstrate that high-energy ball milling alone is effective for particle size reduction and defect generation but insufficient for producing a fully homogeneous $Ni_{50}Ti_{30}Zr_{20}$ alloy within 28 h. Additional activation energy, such as post-milling heat treatment or extended processing, is required to promote complete alloying in this system.

Keywords: high-energy ball milling; NiTiZr; particle size; mechanochemical

Academic Editor: Shouxun Ji

Received: 12 December 2025
Revised: 14 January 2026
Accepted: 15 January 2026
Published: 20 March 2026

1. Introduction

Several methods have been documented for creating NiTiZr intermetallic compounds utilising elemental powders of Ni, Ti, and Zr, including high-energy ball milling [1], self-propagating high-temperature synthesis [2], and explosive shockwave compression [3] of these, ball milling is a productive solid-state powder-processing technique for creating intermetallic compounds. In a high-energy ball-milling process, powder particles are repeatedly cold-welded, fractured, and re-welded. The use of mechanical energy for alloying has existed since the dawn of human civilization [3]. Ball milling is described as a

shear-force-dominated mechano-chemical process [4–6], in which impact and attrition are used to reduce the particle size of a material. A ball mill comprises a hollow cylinder that is filled with balls and fixed to a metallic frame that allows it to spin on its longitudinal axis. The ball diameters are dependent on the mill size and particle size of the feed. The balls occupy 1/3 of the active mill volume, while the other 2/3 is occupied by the NiTiZr powder. Smaller balls contribute to the formation of fine products by filling up the spaces between larger balls, which break down coarse feed material. Pure powders are combined into a single powder by mixing and blending.

The frequency of collisions between the powders and balls depends on the operating parameters, which include powder-to-ball ratio, time, rotation speed of the vessel, and ball size, density, and quantity. Control of milling process parameters is essential for particle size refinement and mechanical alloying. Mhadhbi [6] reported that higher density of grinding media gave a greater reduction in particle size, and a higher rotation speed produced a larger mass of the smallest particles. Friction is an important factor in particle size refinement and alloy formation. Friction between balls can affect material flow, leading to inhomogeneous deformation. The major factor influencing the ball-milling process is ball size. Metallic balls, usually made of steel or zirconia (ZrO_2), serve as grinding media and rotate to generate centrifugal force [7]. The collisions cause the powder particles to break, flatten, and deform. High-energy ball milling is a favourable solid-state method for overcoming the disadvantages of utilising a starting mixture of metallic components with both high and low-temperature melting points [8–15]. The mechanism of particle fracture during ball milling varies with particle size and structure. Ball–powder collisions cause defects such as cracks, which then propagate to form smaller particles, resulting a finer material [16,17]. In this study, a 1 kg blended sample of appropriate relative proportions of nickel, titanium, and zirconium powders was milled in a high-energy ball mill to produce $Ni_{50}Ti_{30}Zr_{20}$. The sample was milled for 28 h under control conditions. Despite previous reports on NiTiZr processing by mechanical alloying, there remains limited consensus on whether complete ternary alloy formation can be achieved by ball milling alone, particularly in systems involving highly reactive elements such as Ti and Zr. Oxide formation, diffusion barriers, and strain-dominated microstructural evolution may strongly inhibit homogenisation. Therefore, the present study aims to systematically investigate microstructural evolution, phase development, and thermal behaviour during high-energy ball milling of $Ni_{50}Ti_{30}Zr_{20}$, with particular emphasis on identifying the limitations of this processing route rather than assuming successful alloy synthesis.

2. Materials and Methods

2.1. Materials

Commercially pure powders supplied by LGC Standards (Teddington, UK) were used. Individual powders of 99.9% Ni (average particle size: 200 μm), 99.9% Ti (0.9–45 μm), and 99.9% Zr (0.9–45 μm) were measured in atomic proportions of 50% Ni, 30% Ti, and 20% Zr, and then blended to give 1 kg of powder.

2.2. Methods

2.2.1. Blending

The dry powders were mixed to homogeneity in a 1 L container and placed in a PerMix 3D mixer (Perfect Mixing Technologies, Chicago, IL, USA) for 10 min at 40 rpm.

2.2.2. Particle Size Analysis

The powders were characterised according to the South African National Accreditation System (SANAS) standard 17025:2017 [18]. The particle size, size distribution, and shapes

of the as-received and milled powders were measured using a particle size distribution (PSD) analyser (Microtrac, FLEX-11.0.0.3, Tokyo, Japan). The obtained particle size was compared with that specified by the supplier.

2.2.3. High-Energy Ball Milling

The 1 kg blended powder was milled in a planetary ball mill (Pulverisette, type 05.202, 250 g vessel, Frisch, Homburg, Germany) using 5 mm and 10 mm diameter stainless-steel balls mixed in 1:2 quantity ratio using a ball-to-powder volume ratio of 10:1 in a dry environment. The milling speed was 200 rpm. The vials holding the powder and the balls were cleaned and purged with high-purity (99.9%) argon gas prior to milling. Milling times ranged from 5 to 28 h. The powders were pyrophoric; therefore, the batches were milled for 1 h and then allowed to cool for 1 h before continuing to maximise process efficiency and avoid overheating. Analysis was performed for samples taken at 2 h intervals. Argon was backfilled into the vessel during sampling to minimise oxidation before milling continued. Fourier Transform Infrared (FTIR) spectroscopy was used to detect the presence of oxides.

2.2.4. Scanning Electron Microscopy

Scanning electron microscopy (SEM) was carried out using a JEOL JSM-6010PLUS/LA instrument (Tokyo, Japan), operated at 20 kV and equipped with an X-ray energy-dispersive spectrometer (EDS) detector. Samples were prepared by placing a small number of particles on conductive carbon tape that was fastened to a specimen mount. Loose debris on the mount was removed using pressurised air. Secondary electron imaging (SEI) mode was used to analyse the morphology and particle size of the powder blend. The powder samples were also mounted in a carbon resin, successively ground to a 15 μm finish, and then polished with oxide polishing suspension on a Struers MD-Chem (Willich, Germany) pad for 7 min. Exposed polished section surfaces of the powder particles were examined by EDS to determine contamination, phase evolution, alloying degree, and chemical homogeneity. Image processing was performed using Image J v1.54k.

2.2.5. Fourier Transform Infrared Spectroscopy (FTIR)

FTIR spectra (Bruker, Alpha 2, Coventry, UK) of the powders were collected to characterise surface chemistry, detect impurities, and assess hydration state. Pellets were prepared using potassium bromide (KBr) as the transparent matrix: approximately 1–2 wt% sample was homogeneously ground with dried KBr, and a 13 mm pellet was formed by pressing at 5–10 tonnes for 1–2 min. Spectra were recorded in transmission mode with 24 scans per sample and averaged to improve signal-to-noise ratio. KBr blanks were run as controls to identify KBr-related features and check for moisture contamination. The resulting spectra were used to identify adsorbed water, hydroxyl, carbonyl and oxide contaminants, and low-frequency metal–oxygen lattice bands.

2.2.6. X-Ray Diffraction

Phase analysis was conducted by X-ray diffraction (XRD) (Malvern Panalytical, Westborough, MA, USA) at room temperature using an X'Pert-PRO powder diffractometer equipped with a PIXcel 3D detector and fixed divergence slit (Malvern Panalytical, Westborough, MA, USA). XRD patterns were recorded in an angular 2θ range from 10° to 110° with a continuous step size of 0.0262° and scan range of 5–90 s/step. A fine focus tube with 45 kV voltage and 40 mA current was used to obtain the incident beam. The resulting diffraction patterns were analysed using Profex software (version 5.0.2).

2.2.7. Differential Scanning Calorimetry

The thermal properties of the powder samples were investigated by differential scanning calorimetry (DSC; DSC1 calorimeter, Mettler Toledo, Columbus, OH, USA), using a crucible with an Al_2O_3 lid in which a hole was punched to release pressure caused by heating. The sample (~20 mg) was heated from room temperature to 600 °C at 0.16 °C/s. A thermocouple measured the temperature and heat flow related to material transitions as a function of temperature and time. A protective atmosphere of nitrogen gas was employed. OriginPro 9.0 was used for redrawing the image. However, the peak temperature and heat released were calculated by the DSC software (STARe Software, version 16.3a).

3. Results and Discussion

3.1. Analysis of As-Received Powders

SEM–SEI micrographs of the initial powders are shown in Figure 1a–c. The nickel particles had spherical morphology (Figure 1a; the Ti and Zr powders had irregular shapes (Figure 1b,c). The mean particle size of the Ni powder was 32.9 µm, with the PSD slightly skewed to the higher diameter range (Figure 1a). The mean particle sizes of the Ti and Zr powders were 88.6 and 52.1 µm, respectively. The Ti micrograph was slightly skewed towards higher PSD; that of Zr displayed an even distribution of powders, with the mean at the centre of the distribution curve. Cumulative distribution curves showed that the largest particles were those of Zr, with a D_{90} of 125.4 µm; the smallest particles were those of Ni, with D_{10} of 5.2 µm (Table 1).

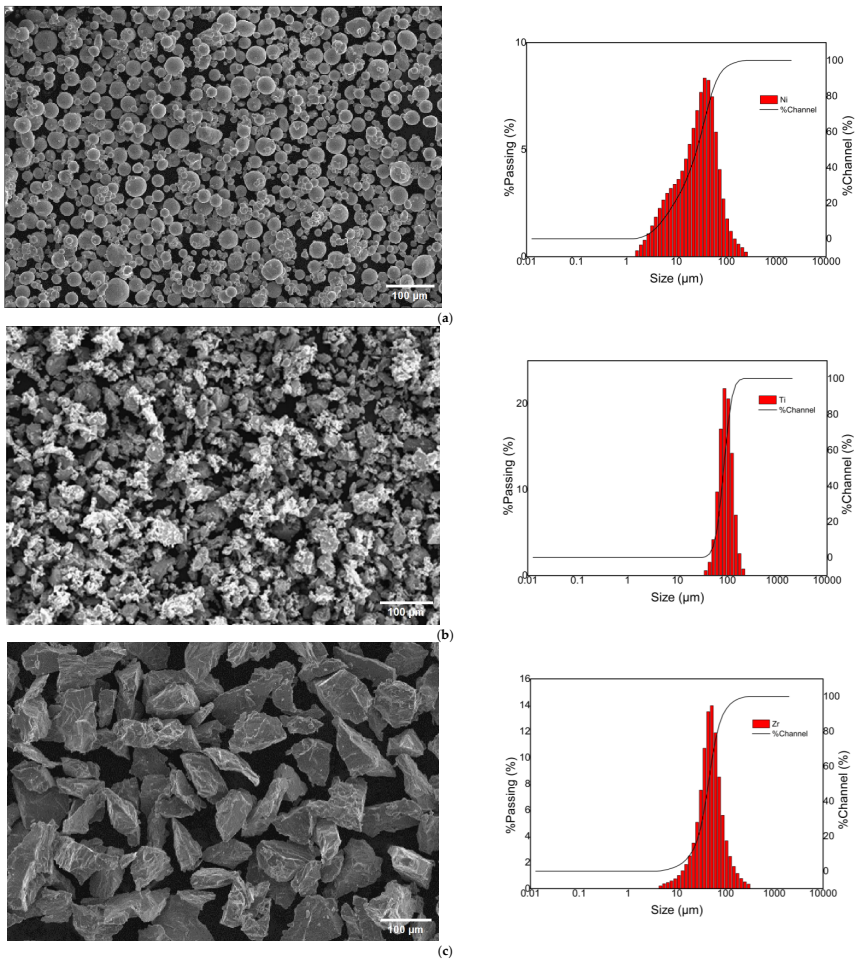

Figure 1. Scanning electron micrographs and particle size distributions of individual elemental powders (**a**) nickel, (**b**) titanium, and (**c**) zirconium.

Table 1. Particle size and particle size distributions of individual metal powders.

	Ni (µm)	Ti (µm)	Zr (µm)
D_{10}	5.21	56.71	19.42
D_{50}	25.76	84.76	44.33
D_{90}	88.23	125.40	90.31
Mean	32.94	88.55	52.12

3.2. Analysis of Blended Powder

The relative mass of each powder required to produce 1 kg of NiTiZr powder of the target composition was calculated. The resulting composition is given in Table 2. Elemental mapping of the blend (Figure 2) confirmed that the actual composition was close to the target.

Table 2. Calculated and actual compositions of blended powder.

Element	Ni	Ti	Zr
Atomic mass (g/mol)	58.69	47.87	91.22
Target (at.%)	50.00	30.00	20.00
Measured (at.%)	52.60 ± 0.26	29.00 ± 0.13	18.50 ± 0.10

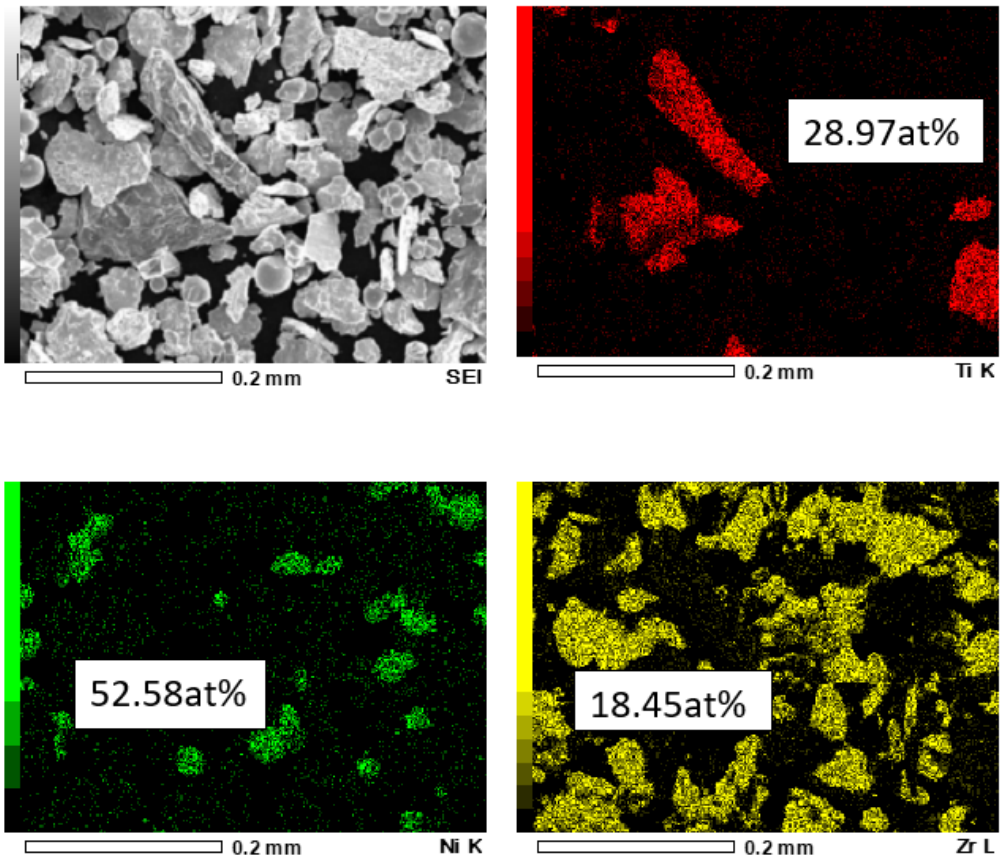

Figure 2. Secondary electron image and elemental analyses of the blended powder.

Additionally, a PSD analysis was performed on the blended powder (Figure 3). The particle shapes of the blended powder varied from irregular to globular, with an average size of 35.08 µm.

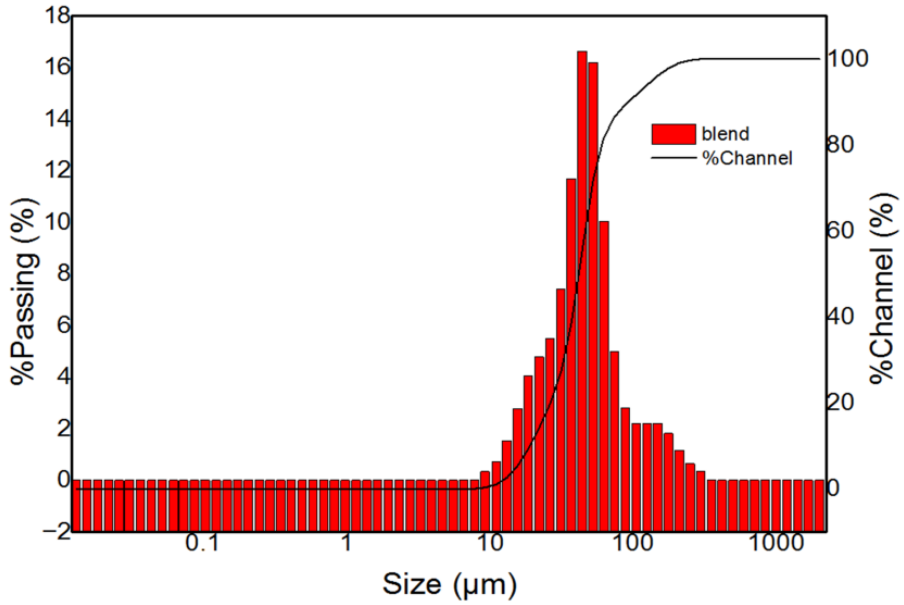

Sizes	Blend (μm)
D_{10}	18.93
D_{50}	41.71
D_{90}	92.09

Figure 3. Particle size distribution curve of the blend.

3.3. Effect of Milling Time on Particle Size

Milling of 250 g of the $Ni_{50}Ti_{30}Zr_{20}$ alloy for 28 h gave an average particle size of 16 ± 1.456 μm (Table 3). Furthermore, two different PSD were produced for 8 h and 16 h milling: The particle sizes reported for 8 h, 16 h and 28 h milling were determined using the equivalent circle diameter (ECD) method using SEM images and processing them in Image J as indicated in Figure 4. At extended milling times (28 h), cold welding dominated over fracture, resulting in severe agglomeration and the formation of large composite particles (up to 120 μm), despite nanoscale crystallite refinement within these particles. This fracture–welding competition explains the apparent non-monotonic particle size trend and is consistent with established mechanical alloying behaviour.

Table 3. Mean size of the powders after milling for 8, 16, and 28 h.

Milling Time (h)	Average Particle Size (μm)
8	30.94 ± 4.691
16	15.32 ± 3.213
28	16 ± 1.456

Particle size refinement was observed after 28 h, but cold-welding caused agglomeration that led to particle sizes up to 120 μm. The significant coarsening of particles measured at 28 h can also be attributed to the more widespread welding and an increase in the crystallite grain size owing to the extended milling time [15–17]. The average particle size after 28 h was 16 ± 1.456. This influence of milling time was compared with that of a 10 g sample of a previously studied binary $Ni_{50}Ti_{50}$ alloy [14] after 100 h milling, the average particle size was ~75 μm. This change in bimodal size fraction with milling time is consistent with observations of ball-milled NiTi [15].

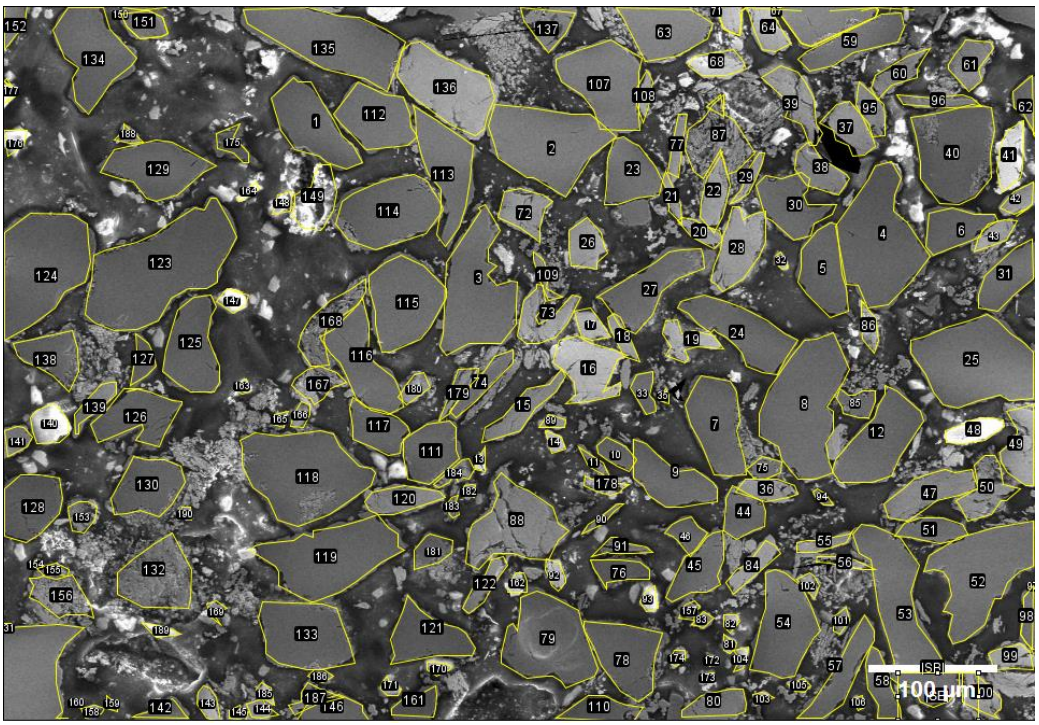

Figure 4. Particle size analysis using the ECD method (8 h).

3.4. Effect of Milling Time on Alloying

The microstructures in Figure 5 show microstructures for 3 samples 8 h, 16 h, and 28 h. For the 8 h sample three compositional phase-contrast domains were easily determined, representing the three distinct elemental powders. At the start of the ball-milling process, the presence of large grey particles is indicative of the low atomic mass element (Ti) (Figure 5a). Ti also had a coarser particle size than Ni. The light (high atomic mass) particles are Zr. The microstructure of the 16 h sample in Figure 5b shows that while the milling process reduced the particle size, it also imparted energy to the alloy; however, this was insufficient to form an amorphous crystal structure With prolonged milling time, the powders reacted to create some homogeneous regions, although the rest of the system remained heterogeneous or polyphasic. At 16 h, preferential fracture and refinement of nickel particles occurred due to their higher ductility. In addition, there were heterogeneous sampling effects during EDS analysis, where Ni-rich regions were locally dominant hence the high amount of nickel in the EDS results for this time.

Homogenous regions showing the presence of Ni, Ti, and Zr indicate the occurrence of reaction between these particles after 28 h milling (Figure 5). The volume fraction of the reacted particles compared to the unreacted ones is approximately 4.6%. The values of each element were determined by EDS and shown in Table 4. In the homogenous regions, Ni and Zr particles became embedded in the ductile Ti particles owing to its plastic deformation. This is because of the ductile nature of the Ti particles; significant plastic deformation and cold-welding were important in later stages of ball milling. Conglomerates, composed of multiple finer, elongated particles with clear borders separating them from one another, were observed at 28 h. The flattened layers tended to overlap, thus forming cold welds, because of the soft starting materials. This observation is consistent with that of other researchers [19,20]. A layered composite particle, comprising a variety of starting materials, then formed over the course of 28 h.

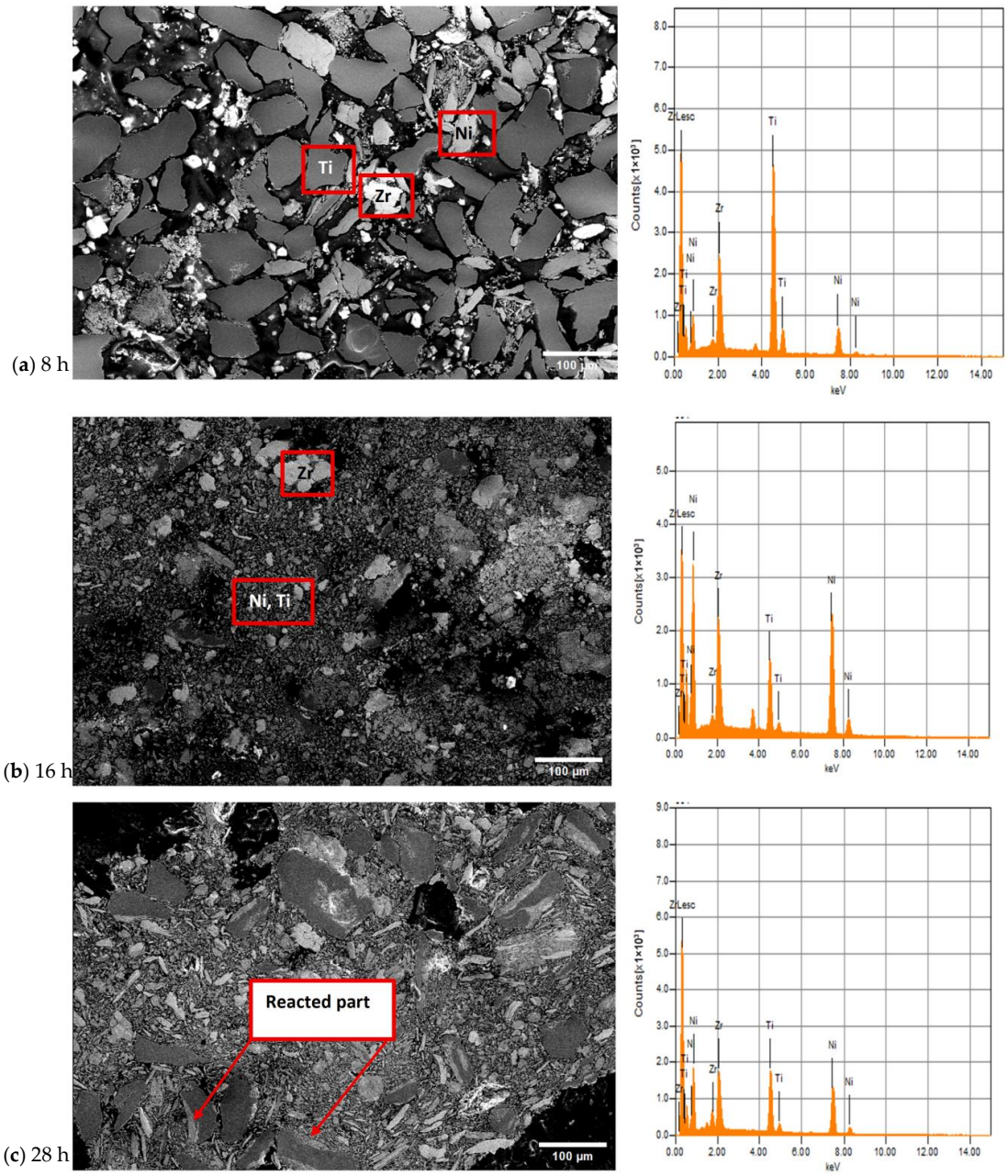

Figure 5. SEM Micrographs and Energy-dispersive X-ray spectroscopy (150×) analyses of blended powder milled for (**a**) 8 h, (**b**) 16 h, and (**c**) 28 h.

Table 4. Atomic mass percentage values of the energy-dispersive spectra in Figure 5.

Milling Time (h)	Ni	Ti	Zr	Total
8	50.47 ± 0.24	31.1 ± 0.12	18.43 ± 0.24	100
16	64.69 ± 0.22	17.69 ± 0.08	17.61 ± 0.20	100
28	48.31 ± 0.24	24.28 ± 0.12	27.41 ± 0.24	100

3.5. Fourier Transform Infrared Spectroscopy (FTIR)

FTIR spectroscopy was employed to identify infrared absorption peaks associated with surface features of the powder. Titanium and zirconium are known to exhibit high reactivity at elevated temperatures. Surface hydroxyl groups were formed through additional hydration of the oxide, likely via secondary reactions with ambient moisture. The vibrational characteristics of titanium oxides and hydroxyl groups differ due to variations in

their molecular surface structures, resulting in distinct infrared absorption peaks. Figure 6 displays a spectrum showing a Ti–O absorption peak at 3400 cm^{-1} and a hydroxyl peak at 1400 cm^{-1}. Given titanium's strong affinity for oxygen, the presence of oxygen-related features in the IR spectrum is expected.

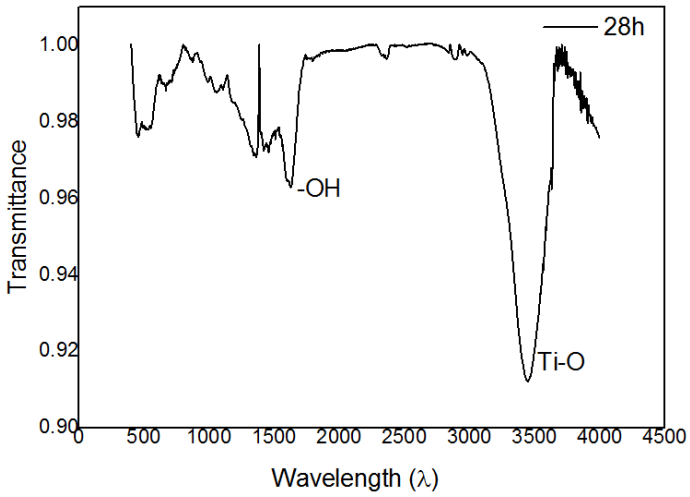

Figure 6. FTIR spectrum of the 28 h powder.

3.6. X-Ray Diffraction

XRD analysis of the powder blend (Figure 7) shows the relative intensities of the different powder components. The respective peaks broadened and became less intense with an increase in milling time. The peak attributed to NiTi-B19 broadened between 0 and 8 h. The mechanical treatment impacted line profiles, and the broadening was anisotropic (Figure 7). Although there are several potential causes of line broadening, size and micro-strain parameters are the most significant [21]. An elevated peak intensity for the peak at 42 2θ (B2-NiTi) signifies a greater quantity of atoms within the crystal, potentially reflecting an increased degree of crystallinity or larger crystal dimensions (Figure 7). The intensity of an XRD peak is proportional to the number of atoms in the crystal that may scatter X-rays: higher peak intensity suggests a larger number of atoms in a crystal, which indicates a higher degree of crystallinity or larger crystal size [22–24]. Although there would be no major alloying due to the absence of changes in the 2θ Bragg locations of the peaks, changes in the crystal lattice as a function of milling time impact peak intensity.

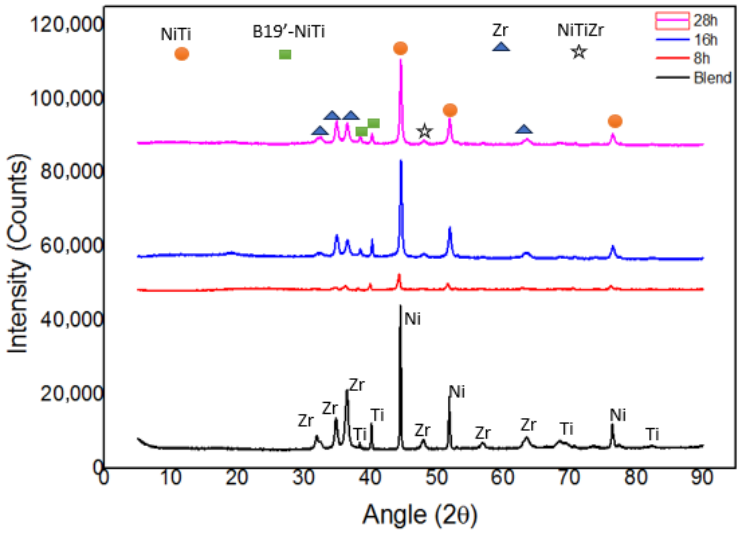

Figure 7. Evolution of X-ray diffraction patterns of powders with milling time.

The refinement spectra shown in Figure 8a corresponds to the initial blended powder of Nickel (Ni), Titanium (Ti), and Zirconium (Zr). The diffraction pattern is characterised by sharp, high-intensity diffraction peaks, which is a direct indicator of high crystallinity and large crystallite size typical of as-received elemental powders. The refinement successfully models the pattern as a simple physical mixture of the constituent elements: face-centred cubic (FCC) Ni, hexagonal close-packed (HCP) Ti, and elemental Zr. The excellent agreement between the observed (black line) and calculated (red line) patterns, evidenced by the near flat difference curve (grey line), confirms the purity of the starting materials and the accuracy of the initial phase model.

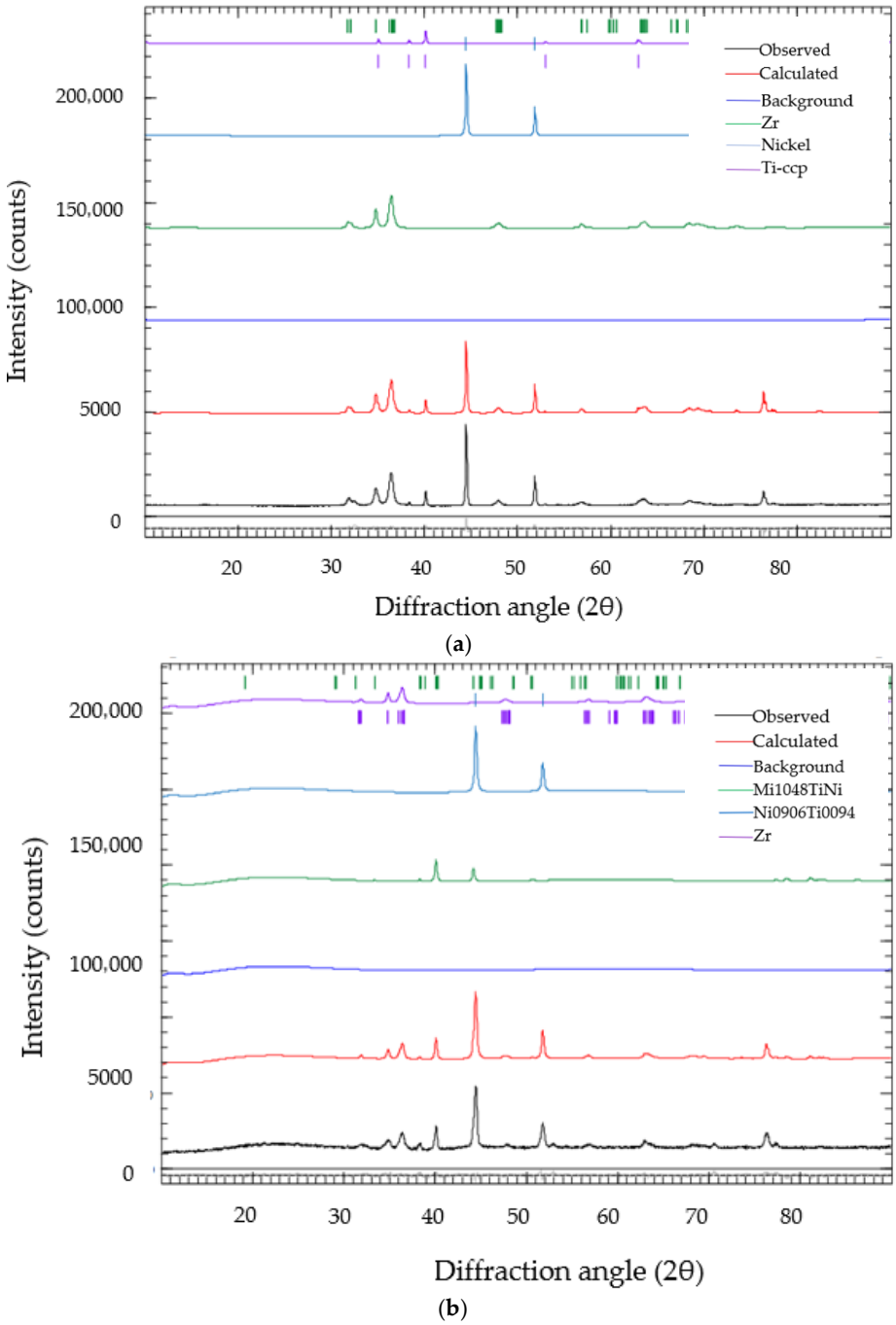

Figure 8. Rietveld refinement of the (**a**) blend and the (**b**) 8 h sample.

In contrast, the second refinement spectra in Figure 8b represents the sample after 8 h of high-energy ball milling, revealing a profound transformation in the material's

microstructure and phase composition. The most striking feature is the significant broadening of the diffraction peaks coupled with a marked decrease in their overall intensity. This phenomenon is the hallmark of severe plastic deformation and nanocrystallisation, where the crystallite size is reduced to the nanometre scale and the internal lattice strain is dramatically increased. Furthermore, the pattern indicates a shift from the simple elemental mixture to a more complex system. While residual peaks from the starting elements may persist, the refinement model incorporates new phases (e.g., the labelled intermetallic or solid solution phases like mp10457201), confirming that the mechanical energy has driven a solid-state reaction.

3.7. Differential Scanning Calorimetry

DSC measurements were used to study transformation temperatures and identify phase transformations. The DSC second run was subtracted and only the first run was reported. Only the forward, or heating, transformation is reported; no peaks were observed for the reverse transformation (Figure 9). The intensity of the detected peaks in DSC analysis can be influenced by the quantity of lattice defects. As a result, depending on the DSC data quality and the curves, the peaks may appear broad. These data were obtained under nitrogen atmosphere, which may have increased the likelihood of nitrification and hence affected the quality of the results. Figure 9 displays DSC curves of the milled alloy powders for various heating times, exothermic thermal events between 300 °C and 470 °C, which are attributed to defect recovery and thermally activated structural rearrangements [25].

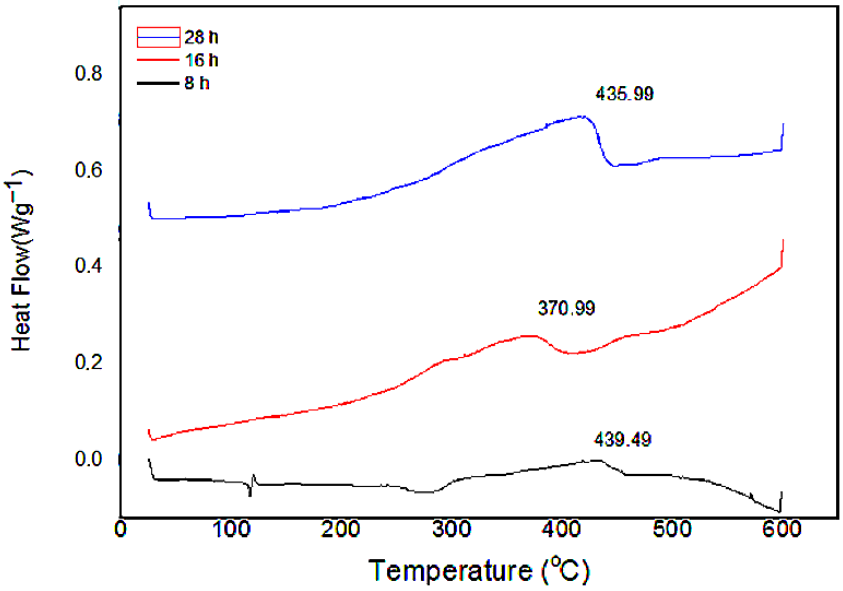

Figure 9. Differential scanning calorimetry curves for powders milled for 8 h, 16 h, and 28 h.

A robust exotherm, centred between 300 °C and 470 °C, was observed in all samples, showing that an exothermic transition due to crystal lattice rearrangement. This accords with the results of a NiTi study conducted by Tian et al. [26] but deviates from those reported by Makifuchi et al. [27]. This peak shows that heat is generated owing to rearrangement of the molecules to a low-energy configuration, which releases energy needed for the molecules to crystallise into the new compound. A peak shift from 436 °C to ~370 °C is observed at 28 h. The shift in peak temperature of the 16 h milled sample to lower temperatures is also characteristic of the existence of other intermetallic compounds inside the material [28,29]. The presence of B2-NiTi intermetallic compounds contributed to the hifted transformation temperatures in the DSC.

Table 5 shows the calculated specific heat capacity of the blended powder increases approximately linearly (from 18.65 to 36.24 to 59.45 Jg^{-1} $°C^{-1}$) as the ball milling duration increases from 8 h to 16 h and then to 28 h. This pattern shows that longer high-energy ball milling progressively modifies the powder (microstructure, size refinement, potential oxidation or phase shifts) so that it can store more heat per unit mass with temperature rise explanation being grain refinement, lattice flaws, and significant plastic deformation are introduced by high-energy ball milling.

Table 5. Specific heat capacity (J/g^{-1} $°C^{-1}$) of the blended powder over time (h).

Time (h)	Cp (Jg^{-1} $°C^{-1}$)
8 h	18.65
16 h	36.24
28 h	59.45

4. Discussion

During the ball milling of the NiTiZr powder, oxide layers of TiO and ZrO_2 form on the outside layer of titanium and zirconium particles due to these elements' high reactivity to oxygen, even under argon purging this happens. This material contains 30% titanium and 20% zirconium; these are high amounts of oxygen-loving elements, and the oxides formed act as diffusion barriers that severely limit interdiffusion of elements. These stable, low-diffusivity oxides (e.g., Ti-O peak at 3400 cm^{-1} confirmed by FTIR) prevent intimate atomic contact, hindering solid-state reactions and contributing to the observed polyphasic microstructure after 28 h of milling. Zirconium exhibits particularly sluggish solid-state diffusion kinetics owing to its high melting point (1855 °C) and large atomic radius, which restrict atomic mobility in the Ni-Ti matrix during milling-induced deformation [30]. Thermodynamic stability of elemental lattices and localised adiabatic heating from ball impacts (up to several hundred °C transiently) further constrain diffusion, favouring defect accumulation over complete homogenisation, as evidenced by peak broadening in XRD without 2θ shifts.

Competing cold welding and fracture dominates the ball milling process: ductile nickel and titanium promote welding into layered composites, while brittle zirconium fractures, enabling mechanical mixing but not chemical alloying, resulting in only 4.6% reacted regions [31].

5. Conclusions

The following conclusions were drawn from the findings of this research:

(1) High-energy ball milling Ni, Ti and Zr for 28 h alone fails to achieve full NiTiZr alloy formation due to persistent oxide diffusion barriers (TiO/ZrO_2), Zr's sluggish diffusivity from its high melting point, localised heating favouring defects over diffusion, and competing cold welding/fracture that yields only mechanical mixing.
(2) Alloying remains partial, with merely 4.6% homogeneous Ni-Ti-Zr regions after 28 h of milling.
(3) However, nanocrystalline refinement (~10 nm), high lattice strain, and polyphasic powders lacking bulk NiTiZr phases were observed, as indicated by XRD broadening.
(4) There were homogeneous and inhomogeneous regions of the powders as displayed in the SEM micrographs.
(5) The powder milled for a longer period resulted in exothermic reactions.

6. Future Research

Post-milling heat treatments such as vacuum/inert annealing (400–600 °C) can recover defects and drive phase evolution. This is recommended for the mechanical alloying and formation of the NiTiZr alloy. To further promote alloying, a controlled post-milling annealing treatment under vacuum or an inert atmosphere in the temperature range of approximately 300–600 °C can be employed [32]. Such thermal treatment facilitates the recovery of milling-induced defects and enhances atomic diffusion, which may activate exothermic structural rearrangements consistent with the DSC peaks observed between 370 and 436 °C. In addition, spark plasma sintering (SPS) offers a promising consolidation route, as it enables rapid heating under applied pressure, achieving high densification while suppressing excessive grain growth [33]. This approach is particularly advantageous for promoting phase formation in mechanically alloyed NiTiZr systems. Furthermore, reactive milling using process control agents (PCAs), such as stearic acid, can effectively reduce cold welding, refine particle size, and limit oxidation, thereby improving compositional homogeneity prior to subsequent annealing treatments [34,35].

Author Contributions: T.P.S.: Conceptualisation, methodology, writing—original draft, writing—review and editing. M.N.M.: Writing—review and editing, formal analysis, funding acquisition, supervision. C.W.S.: Funding acquisition, supervision, methodology, validation, formal analysis. All authors have read and agreed to the published version of the manuscript.

Funding: This work was supported by the National Research Foundation in South Africa under the Competitive Support Grant (Ref no: CSUR240508217931).

Data Availability Statement: All original contributions from the study are contained within the article. Additional inquiries can be addressed to the corresponding author.

Acknowledgments: The National Laser Centre at the Council for Scientific and Industrial Research (South Africa) and the University of Pretoria financially supported this work. K.C. Sole carried out English editing of this manuscript.

Conflicts of Interest: The authors declare that none of the work reported in this study could have been influenced by any known competing fiscal interests or personal relationships.

References

1. Takasaki, A. Mechanical Alloying of the Ti–Ni System. *Phys. Status Solidi* **1999**, *169*, 183–191. [CrossRef]
2. Jarfors, A.W.E.; Sim, G.C.; San, T.E. Influence of Process Parameters on Reaction Products during Self-Propagating High-Temperature Synthesis of Porous NiTi. *Mater. Sci. Forum* **2003**, *437–438*, 475–478. [CrossRef]
3. Sopicka-Lizer, M. *High-Energy Ball Milling: Mechanochemical Processing of Nanopowders*; CRC: Boca Raton, FL, USA; Woodhead Publishing Limited: Cornwall, UK, 2010.
4. Benjamin, J.S. Mechanical Alloying—A Perspective. *Met. Powder Rep.* **1990**, *45*, 122–127. [CrossRef]
5. Babalola, B.J.; Shongwe, M.B.; Rominiyi, A.L.; Jeje, S.O.; Olubambi, P.A. A Study of Nanocrystalline Nickel Powders Developed via High-Energy Ball Milling. *Int. J. Adv. Manuf. Technol.* **2019**, *102*, 3657–3665. [CrossRef]
6. Mhadhbi, M. Modelling of the High-Energy Ball Milling Process. *Adv. Mater. Phys. Chem.* **2021**, *11*, 31–44. [CrossRef]
7. Çakar, H.U. Production of Zirconia Powders by Milling Process. Master's Thesis, Marmara Universitesi, Istanbul, Turkey, 2013.
8. Suryanarayana, C. Mechanical Alloying and Milling. *Prog. Mater. Sci.* **2001**, *46*, 1–184. [CrossRef]
9. Zhang, Y.; Jiang, S.; Zhu, X.; Zhao, Y.; Liang, Y.; Sun, D. Influence of Fe Addition on Phase Transformation Behavior of NiTi Shape Memory Alloy. *Trans. Nonferrous Met. Soc. China* **2017**, *27*, 1580–1587. [CrossRef]
10. Guessasma, S.; Zhang, W.; Zhu, J.; Belhabib, S.; Nouri, H. Challenges of Additive Manufacturing Technologies from an Optimisation Perspective. *Int. J. Simul. Multidiscip. Des. Optim.* **2015**, *6*, A9. [CrossRef]
11. Zhang, D.L. Processing of Advanced Materials Using High-Energy Mechanical Milling. *Prog. Mater. Sci.* **2004**, *49*, 537–560. [CrossRef]
12. Koch, C.C.; Whittenberger, J.D. Mechanical Milling/Alloying of Intermetallics. *Intermetallics* **1996**, *4*, 339–355. [CrossRef]
13. Koch, C.C. Synthesis of Nanostructured Materials by Mechanical Milling: Problems and Opportunities. *Nanostruct. Mater.* **1997**, *9*, 13–22. [CrossRef]

14. Salwa, P.; Goryczka, T. Crystallization of Mechanically Alloyed $Ni_{50}Ti_{50}$ and $Ti_{50}Ni_{25}Cu_{25}$ Shape Memory Alloys. *J. Mater. Eng. Perform.* **2020**, *29*, 2848–2852. [CrossRef]
15. Goryczka, T.; Salwa, P. Influence of Batch Mass on Formation of NiTi Shape Memory Alloy Produced by High-Energy Ball Milling. *Metals* **2021**, *11*, 1908. [CrossRef]
16. Dash, A.S.; Manna, I.; Devapal, D.; Sharma, S.C.; Majumdar, J.D. Effect of Process Parameter on the Flowability of Nanocrystalline CoNiCrAlY Powder Synthesized by Mechanical Milling. *Particuology* **2024**, *92*, 210–223. [CrossRef]
17. Mhadhbi, M.; Khitouni, M.; Azabou, M.; Kolsi, A. Characterization of Al and Fe Nanosized Powders Synthesized by High Energy Mechanical Milling. *Mater. Charact.* **2008**, *59*, 944–950. [CrossRef]
18. *ISO/IEC 17025:2017*; General Requirements for the Competence of Testing and Calibration Laboratories. SANAS: Washington, DC, USA, 2017. Available online: https://www.iso.org/obp/ui/en/#iso:std:iso-iec:17025:ed-3:v1:en (accessed on 8 September 2025).
19. Mahlatji, M.L.; Chikosha, S.; Chikwanda, H.K.; Stumpf, W.E.; Siyasiya, C.W. Formation of Amorphous Ti-50 at.% Pt by Solid-State Reactions during Mechanical Alloying. *J. S. Afr. Inst. Min. Metall.* **2014**, *114*, 167–172.
20. Sharma, N.; Raj, T.; Jangra, K.K. Microstructural Evaluation of NiTi-Powder, Steatite, and Steel Balls After Different Milling Conditions. *Mater. Manuf. Process.* **2016**, *31*, 628–632. [CrossRef]
21. Arunkumar, S.; Kumaravel, P.; Velmurugan, C.; Senthilkumar, V. Microstructures and Mechanical Properties of Nanocrystalline NiTi Intermetallics Formed by Mechanosynthesis. *Int. J. Miner. Metall. Mater.* **2018**, *25*, 80–87. [CrossRef]
22. Soleimanian, V.; Aghdaee, S.R. Comparison Methods of Variance and Line Profile Analysis for the Evaluation of Microstructures of Materials. *Powder Diffr.* **2008**, *23*, 41–51. [CrossRef]
23. Huang, J.Y.; Wu, Y.K.; Ye, H.Q. Ball Milling of Ductile Metals. *Mater. Sci. Eng. A* **1995**, *199*, 165–172. [CrossRef]
24. Enayati, M.H.; Mohamed, F.A. Application of Mechanical Alloying/Milling for Synthesis of Nanocrystalline and Amorphous Materials. *Int. Mater. Rev.* **2014**, *59*, 394–416. [CrossRef]
25. Li, B.; Zheng, L.J.; Zhang, H. Microstructure-Property Relationship in Zr-Alloyed Ni-Rich NiTi Alloys: Enhancements in High-Temperature Stability and Superelasticity. *Mater. Charact.* **2024**, *208*, 113649. [CrossRef]
26. Vedamanickam, S.; Vageeswaran, P.; Jacob, B. Theoretical Analysis and Design of Ti-Based Shape Memory Alloys Correlating Composition and Electronic Properties to Transformation Temperatures for High Temperature Applications. *Mater. Sci. Eng. B* **2023**, *296*, 116681. [CrossRef]
27. Tian, B.; Tong, Y.X.; Chen, F.; Liu, Y.; Zheng, Y.F. Phase Transformation of NiTi Shape Memory Alloy Powders Prepared by Ball Milling. *J. Alloys Compd.* **2009**, *477*, 576–579. [CrossRef]
28. Makifuchi, Y.; Terunuma, Y.; Nagumo, M. Structural Relaxation in Amorphous Ni-Ti Alloys Prepared by Mechanical Alloying. *Mater. Sci. Eng. A* **1997**, *226–228*, 312–316. [CrossRef]
29. Carl, M.; Smith, J.; Van Doren, B.; Young, M. Effect of Ni-Content on the Transformation Temperatures in NiTi-20 at.% Zr High Temperature Shape Memory Alloys. *Metals* **2017**, *7*, 511. [CrossRef]
30. Hou, J.; Gan, J.; Wang, T.; Luan, J.; Zhang, T.; Ren, Z.; Zhang, Z.; Wen, W.; Wang, Z.; Song, W.; et al. Anomalous Temperature Dependence of Yield Strength and Deformation Mechanisms in Chemically Complex Intermetallic Alloy. *Mater. Sci. Eng. A* **2025**, *931*, 148211. [CrossRef]
31. Zang, D.; Becker, J.; Betke, U.; Hasemann, G.; Khanchych, K.; Gorr, B.; Krüger, M. Phase Evolution During High-Energy Ball Milling and Annealing of Ti-Doped Mo-V-Si-B Alloys. *Materials* **2025**, *18*, 2494. [CrossRef]
32. Bodunde, O.P.; Gao, S.; Qu, S.; Ding, J.; Song, X.; Liao, W.H. Mitigating functional fatigue of 3D-printed nickel-titanium shape memory alloy using hybridizing stabilizers. *Results Eng.* **2025**, *27*, 106440. [CrossRef]
33. Guo, Y.; Liu, M.; Jiang, C.; Liu, R.; Zhang, J.; Liu, Y.; Wang, Z.; Li, H.; Sha, P.; Xin, R.; et al. Effect of Annealing on the Transformation Temperatures and Shape Memory Effect of Laser Powder Bed Fusion Niti Alloy. 2023. Available online: https://ssrn.com/abstract=4658584 (accessed on 8 December 2025).
34. Le Godec, Y.; Le Floch, S. Recent developments of high-pressure spark plasma sintering: An overview of current applications, challenges and future directions. *Materials* **2025**, *16*, 997. [CrossRef]
35. Amadi, A.; Mohyaldinn, M.; Ridha, S.; Ola, V. Advancing engineering frontiers with NiTi shape memory alloys: A multifaceted review of properties, fabrication, and application potentials. *J. Alloys Compd.* **2024**, *976*, 173227. [CrossRef]